Visible-near infrared ultra-broadband polarization-independent metamaterial perfect absorber involving phase-change materials

Ximin Tian and Zhi-Yuan Li*

Laboratory of Optical Physics, Institute of Physics, Chinese Academy of Science, P.O. Box 603, Beijing 100190, China
**Corresponding author: lizy@aphy.iphy.ac.cn*

Received June 8, 2016; revised June 22, 2016; accepted June 23, 2016;
posted June 24, 2016 (Doc. ID 267933); published July 19, 2016

We numerically demonstrate a novel ultra-broadband polarization-independent metamaterial perfect absorber in the visible and near-infrared region involving the phase-change material $Ge_2Sb_2Te_5$ (GST). The novel perfect absorber scheme consists of an array of high-index strong-absorbance GST square resonators separated from a continuous Au substrate by a low-index lossless dielectric layer (silica) and a high-index GST planar cavity. Three absorption peaks with the maximal absorbance up to 99.94% are achieved, owing to the excitation of plasmon-like dipolar or quadrupole resonances from the high-index GST resonators and cavity resonances generated by the GST planar cavity. The intensities and positions of the absorption peaks show strong dependence on structural parameters. A heat transfer model is used to investigate the temporal variation of temperature within the GST region. The results show that the temperature of amorphous GST can reach up to 433 K of the phase transition temperature from room temperature in just 0.37 ns with a relatively low incident light intensity of 1.11×10^8 W/m^2, due to the enhanced ultra-broadband light absorbance through strong plasmon resonances and cavity resonance in the absorber. The study suggests a feasible means to lower the power requirements for photonic devices based on a thermal phase change via engineering ultra-broadband light absorbers.

OCIS codes: (160.3918) Metamaterials; (190.4870) Photothermal effects; (240.6680) Surface plasmons; (140.3945) Microcavities; (300.1030) Absorption; (320.7080) Ultrafast devices.
http://dx.doi.org/10.1364/PRJ.4.000146

1. INTRODUCTION

Since creatively proposed by Landy *et al.* [1], the concept of metamaterial perfect absorbers (MMPAs) has initiated several new research fields such as photodetectors [2], photovoltaics [3,4], sensors [5–7], etc., owing to their near unity absorbance, broadband, and polarization-independent merits. As is well known, MMPAs are resonant metallic nanostructures with unit cells much smaller than the operating wavelength of light [8–11], in which the fundamental principle is to minimize the reflectance through impedance matching with free space [1,12] and to eliminate the transmittance by maximizing the metamaterial losses [1]. As the electric and magnetic resonant frequencies of MMPAs are determined by their geometry, the conventional MMPAs can only produce certain electric and magnetic resonances at the specific wavelengths [13], which restricts their practical applications. For this, several schemes concentrating on dual-band absorption [14–16], multiband absorption [17,18], and broadband light absorption at terahertz frequencies [19–24] generated by MMPAs have been demonstrated, which are more conducive to high-integration optoelectronic applications. For instance, Cui *et al.* [21] have demonstrated an ultra-broadband thin-film infrared absorber made of saw-toothed anisotropic metamaterial by etching an MM slab into a sawtooth shape with the tooth widths increasing gradually from top to bottom. In another example, Hu *et al.* [24] reported that the trapping "rainbow" storage of light with metamaterials and plasmonic graded surface gratings produces broadband light absorption by controlling the velocity of light in guided photonic structures. Nevertheless, these structures inevitably become increasingly complex when two or more sub-resonators operating at different wavelengths are compacted in a composite unit cell for the multispectral absorption, which limits practical device applications. To date, although much effort on MMPAs has been proposed, there have been only a few attempts to realize ultra-broadband MMPAs at the visible and near-infrared region via a fairly straightforward process [13] because the resonant elements whose sizes are much smaller than the resonant wavelength are difficult to realize experimentally [25].

Recently, phase-change materials (PCMs), such as VO_2 and $Ge_2Sb_2Te_5$ (GST), representing one of the best candidates for future electronic FLASH memory, have been widely used in commercial optical disks and rewritable optical data storage media [26,27]. Moreover, PCMs also have been demonstrated in both nonplasmonic [11,12] and plasmonic [13–18] absorbers. As one of the most active PCMs, GST can exhibit an amorphous-to-crystalline phase transition that can be electrically, thermally, or optically manipulated. Generally, the temperature-controlled phase transition of GST is much more preferable due to the nonvolatile property at room temperature and the large contrast of refractive index between different states. Meanwhile, GST also is investigated to show the advantages of a short time (10 ns irradiated by a focused laser) [28] and a lower total optical power or energy [29,30] for amorphous-to-crystalline transition. Notably, GST has large real and imaginary parts of a refractive index over the entire

visible spectra, indicating that it is beneficial to construct a high-index microcavity platform and generate broadband strong absorption by utilizing appropriate structural systems. These advantages suggest that GST could be used to achieve ultra-broadband MMPAs in the visible wavelength region.

In this article, by going beyond the conventional restrictions using metallic or dielectric array as resonators [13–15,31–33], we attempt to introduce the PCM GST as plasmon-like resonators in MMPAs. Meanwhile, we integrate a high-index planar thin film cavity of GST within the MMPA to boost light absorption. In detail, the novel MMPA is composed of an array of GST resonators separated from a continuous Au substrate by a silica spacer and a high-index GST planar cavity. Herein, the GST resonators are used to provide dipole or quadrupole resonances, and the GST planar cavity is exploited to support cavity modes. By optimizing the structural parameters, we theoretically show that this MMPA yields three absorption peaks with more than 99% absorbance in the wavelength range from 350 to 1500 nm. Additionally, this MMPA also achieves ultra-broadband, polarization-independent absorption properties. The integrated absorption of the MMPA reaches up to 92.9% over the entire light spectra, which has never been achieved by previous simple schemes of design. A heat model is then constructed to investigate the temporal variation of the temperature of the GST region of the MMPA. The results show that the temperature of GST can be raised from room temperature to >481 K in just 0.56 ns with a relatively low incident light intensity of 1.11×10^8 W/m^2. Hence, such a unique MMPA could be capable of lowering the power requirements for MMPAs based on the thermal phase change, paving the way for the realization of ultrafast photothermal switches, optical storage, solar energy conversion, ultrafast thermophotovoltaic technology, and so on.

2. DESIGN MODEL AND SIMULATION METHOD

Figure 1(a) shows the structure of the proposed MMPA, where the high-index PCM GST square resonator array is on the top of the low-index dielectric spacer of silica and acts as plasmon-like resonators. The GST resonators are arranged in a square lattice, so that the optical response from this absorber is polarization-independent [13,34]. The width (w) and the period (p) of the square resonators are set to be 160 and 300 nm, respectively. The thickness of the resonators (h) and the silica spacer film (t) are 60 and 30 nm, respectively. Subsequently, a GST film with 180 nm in thickness (denoted by T) underneath the silica spacer is sputtered on top of Au substrate with 100 nm in thickness, which ensures that transmission of the structure is totally eliminated. The whole structure resides on a 200 um thick BK7 glass.

A 3D finite-difference time-domain (FDTD) method is employed to simulate the optical properties of the absorber. Taking the periodic nature of the metamaterial absorber into account, the model boundary at $x = p/2$ and $y = p/2$ is set to satisfy a periodic condition. Perfectly matched layers (PML) are implemented at the upper and bottom boundary of the model. The totally flat white light with a wavelength range from 350 to 1500 nm propagates along the negative z direction and the E field is polarized in the x direction with an amplitude of E_0. The optical constant of Au is taken from

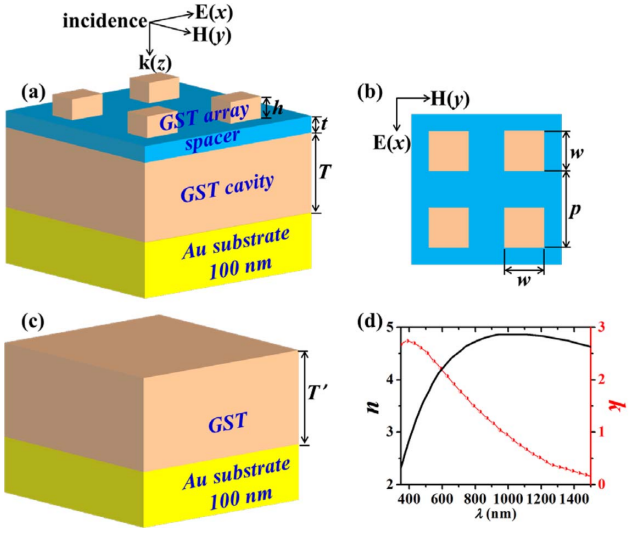

Fig. 1. (a) 3D schematic diagram of the proposed MMPA and the incident light polarization configuration. The thicknesses of GST square resonators, silica spacer, and GST planar cavity are $h = 60$ nm, $t = 30$ nm, and $T = 180$ nm, respectively. The lattice period in both x and y directions is $p = 300$ nm, and the edge of the square resonator is $w = 160$ nm. (b) Top view of the proposed MMPA showing the structural parameters. (c) 3D schematic diagram of the planar control device as a comparison, where the thicknesses T' of GST is tunable to guarantee its volume equally to that of the MMPA. (d) Real n (solid line, black) and imaginary k (sample line, red) parts of the refractive index for the amorphous phase of GST.

the data of Palik [35]. The refractive index of silica is set to 1.45. The refractive index of GST in the amorphous phase is obtained from the experimental data in [36], shown in Fig. 1(d). It is found that the dielectric constant of GST is dispersive, and the real and imaginary parts of the refractive index of GST are both large in the visible and near-infrared region (NIR) band. As a result, the resonators of GST can be utilized to yield significant optical field coupling with the incident light and lead to strong absorption by the dissipative GST material. The standard deposition technique [37] and the well-developed laser interference lithography (LIL) with dry etching method [38] can be applied to fabricate the proposed MMPA architecture.

3. ABSORPTION ENHANCEMENT FOR MMPA

Figure 2 presents the calculated reflectance [donated by *Ref.*, panel (a)] along with absorbance [donated by *Abs*, panel (b)] for this proposed MMPA at the normal TM (or TE) polarized light, where $p = 300$ nm, $w = 160$ nm, $h = 60$ nm, $T = 180$ nm, and $t = 30$ nm, respectively. Simultaneously, the corresponding spectra of a reference planar control device also are given for comparison. As can be seen, the MMPA exhibits three near-zero reflection dips owing to impedance matching to the vacuum, leading to three strong absorption peaks with absorbance of 99.8%, 99.2%, and 99.9% at the wavelength of $\lambda_1 = 425$ nm, $\lambda_2 = 753$ nm, and $\lambda_3 = 1325$ nm, respectively. On the contrary, for the planar control device, its absorbance curve is nearly flat with a low absorbance of 52% across the wavelength range from 350 to 900 nm and only shows one absorption peak at the wavelength of 1400 nm. To be more intuitive, the integrated absorbance for the MMPA and the

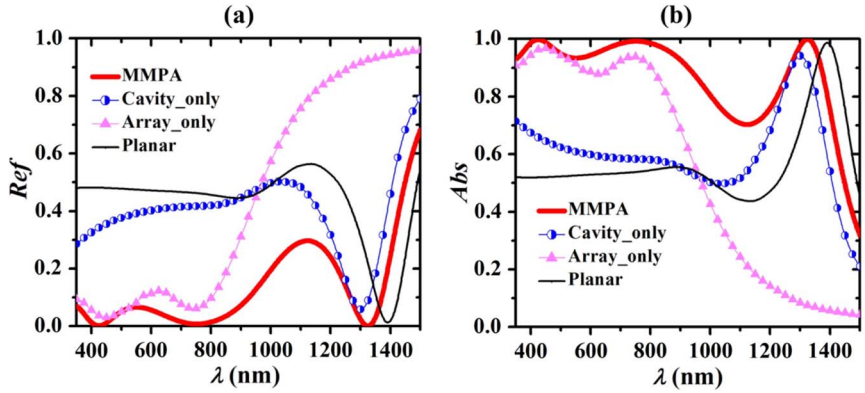

Fig. 2. 3D FDTD simulation of spectra of (a) reflectance and (b) absorbance for the proposed MMPA, the device with only GST planar cavity, the device with only GST square resonators, and the planar control device with the amorphous GST under the illumination of normal incidence light, respectively.

planar control device with equivalent GST volume is calculated, which are 92.92% and 56.96%, respectively. That is to say, the integrated absorbance of the proposed MMPA is increased by 63.13% over the whole wavelength range compared with that of the planar control one, indicating the proposed MMPA is a highly efficient device for light energy absorption and harvesting. Here, the equivalent GST volume refers to the volume of GST for the MMPA, $T \times p^2 + h \times w^2$, which equals to that for the planar control device, $T' \times p^2$.

To gain insight into the effect of the plasmon-like resonators and GST planar cavity on broadening the absorbance spectrum, we alternatively calculate the normalized electric field distributions of the MMPA structures upon normal incidence at the resonant peaks, and the results are shown in Figs. 3(a)–3(c). Being analogous to the above-mentioned configurations with metallic resonators [13,29,34,39], the top GST square resonator array replacing the metallic resonator square array within the MMPA can generate electric dipolar/quadrupole resonances. The electric field at λ_1 is mainly confined at the two top corner areas of the GST resonators and the gap areas between the top resonators and the bottom cavity; thus, it is attributed to the excitation of the dipolar resonance. Meanwhile, the electric fields at λ_2 and λ_3 are primarily concentrated in the corner areas of the GST resonators and are attributed to the excitation of quadrupole resonance. The pronounced distinction between the electric field distributions at λ_2 and λ_3 is that strong cavity resonance emerges at λ_3, which dramatically broadens the absorption spectrum in the NIR band. To further verify the nature of absorption enhancement, the reflectance and absorbance spectra for the configurations

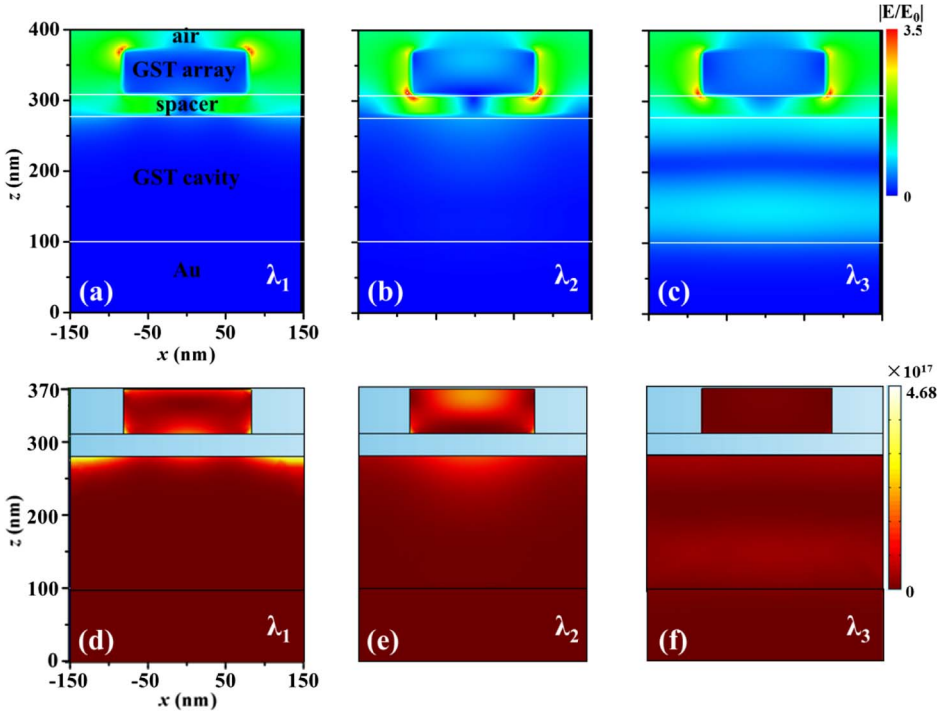

Fig. 3. (a–c) Normalized electric field distributions and the (d–f) heat power volume density Q_d of the absorption peaks at $\lambda_1 - \lambda_3$ for the proposed MMPA with amorphous phase of GST at normal incidence, respectively. The Q_d is in unit of W/m^3.

with only the GST resonators (without the GST planar cavity) or with only the GST planar cavity (without the GST resonators) are also shown in Fig. 2. These spectra indicate that the GST resonators contribute to the absorption enhancement in the visible band, and the GST planar cavity accounts for the near-perfect absorbance in the NIR band.

The lossy nature of GST, manifested by its large imaginary part of refractive index, implies that resistive heat will be generated in the GST metamaterial absorber. The heat power volume density Q_d is written as [39]

$$Q_d = \frac{1}{2}\varepsilon_0 \omega \,\mathrm{Im}(\varepsilon_r)|E|^2, \tag{1}$$

where ε_0 is permittivity of vacuum, ω is the angular frequency of the illuminating light, ε_r represents the relative permittivity of amorphous GST, and E is the amplitude of electric field within the nanostructure. Figures 3(d)–3(f) show the calculated heat power volume density Q_d distributed within the proposed structure at the resonances of λ_1, λ_2, and λ_3 with the same scale bar under the irradiation of laser pulse with intensity of 1.11×10^8 W/m^2 (the maximum Q_d are up to 4.68×10^{17}, 3.38×10^{17}, and 4.36×10^{16} W/m^3 at λ_1, λ_2, and λ_3, respectively). Furthermore, we can find that the dominant portion of heat source is localized at the top GST array and the upper parts of the GST planar cavity at λ_1 and λ_2. Distinctively at the resonances of λ_3, the generated heat is mainly confined in the area of constructive interference within the GST planar cavity. All these features coincide with the behaviors of the aforementioned optical absorption enhancement and indicate that the plasmon resonance induced by the GST resonators accompanied with cavity resonance formed within the GST planar cavity obviously boosts the heat power generation and localization during the photothermal process.

In order to know how the geometrical parameters of the MMPA, including the period (p) and the width (w) of the nanopatterned array, and the thickness (T) of the GST planar cavity, affect the mode resonances, we perform numerical simulations of the hybrid MMPA, in which only one parameter is variable and the others are kept unchanged. Here, by default, $p = 300$ nm, $w = 160$ nm, and $T = 180$ nm, and other involved geometrical parameters are fixed such that $h = 60$ nm and $t = 30$ nm, respectively.

Figure 4(a) presents the absorption maps as a function of the wavelength and the period p of the MMPA device at the normal incidence case. As the period p increases, the absorbance at λ_1 and λ_2 is obviously suppressed. Moreover, the absorption band at λ_1 redshifts and that at λ_2 significantly blueshifts, leading to the spectral lineshape in the visible wavelength range extremely narrowed down. This feature probably stems from the weakened optical coupling between the adjacent GST resonators. On the contrary, with increasing the GST resonator size, the absorption spectrum in the visible wavelength range shows distinct responses, gradually splitting into two absorption bands at λ_1 and λ_2 [shown in Fig. 4(b)], which are probably due to the enhanced optical coupling between the GST resonators. Simultaneously, as the width w of the nanopatterned GST array increases, the absorption band at λ_2, originating from the quadrupole resonance mode, redshifts gradually to approach and couple with the cavity modes at λ_3. Particularly, the spectral position at λ_3 is almost fixed due to the excitation of the cavity mode, which is independent of the period and width of the GST array.

In general, the resonant frequency of a planar Fabry–Perot (F–P) cavity mode is determined by the formula [40]:

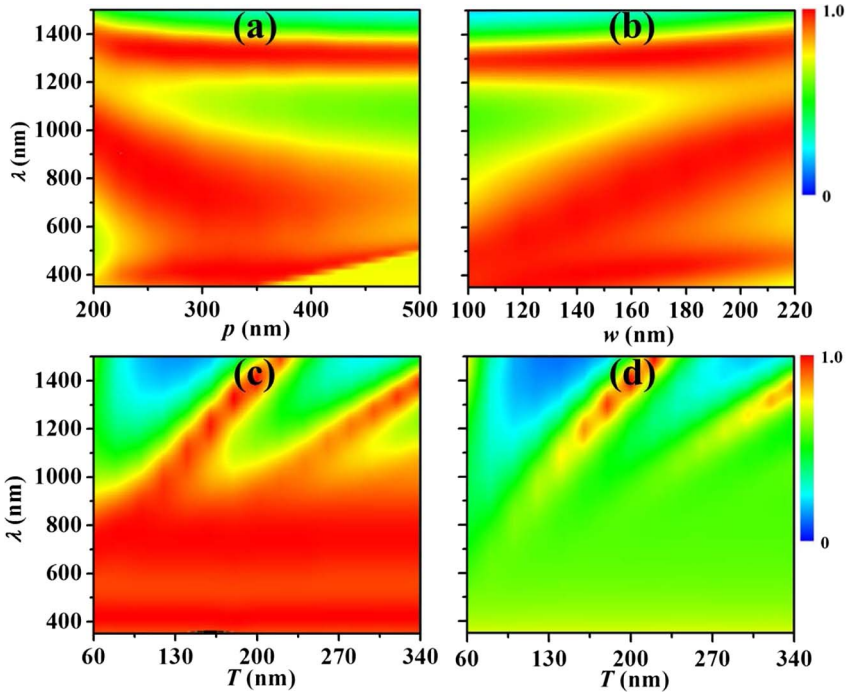

Fig. 4. Contour plot of the absorption spectrum dependence on the (a) lattice period p, the (b) square dimension w, and the (c) thicknesses T of GST planar cavity, respectively. Herein, the other structural parameters are the same as those of Fig. 1(a). The absorption evolution versus the thicknesses of GST planar cavity for the control device with only GST planar cavity also is depicted in panel (d) as a comparison.

$$2k_{\text{eff}}T + \varphi_t + \varphi_b = 2m\pi. \quad (2)$$

Here k_{eff} is the effective wave vector of the GST planar cavity, φ_t and φ_b represent the phase shifts at the top and bottom faces of this cavity, and m is a positive integer. Figure 4(c) demonstrates the dependence of absorption spectrum on the incident wavelength and the thickness T of the GST cavity. It is found that the thickness T of the GST cavity has little effect on the absorption spectrum in the visible wavelength range. However, the spectral lineshape of the cavity resonance in the NIR band can be sensitively dependent on T. As T increases under the condition of $T < 200$ nm, the wavelength of fundamental resonance redshifts approximately linearly as expected, where the contribution of the phase shift can be ignored compared with the F–P mode [41]. When T exceeds 200 nm, other absorption bands corresponding to higher-order cavity resonances emerge. These findings again confirm the great contributions to the MMPA from the optical resonances supported by the GST cavity. Alternatively, the absorption versus T and wavelength for the control configuration with only the GST planar cavity also are investigated, and the result is displayed in Fig. 4(d). It can be observed that the excited cavity resonance is drastically reduced in strength compared with that for the proposed MMPA, which implies the top GST resonators also play a pronounced role of efficiently harvesting the incident light into the MMPA device.

4. FAST PHASE TRANSITION OF $Ge_2Sb_2Te_5$

As is well-known, GST is a prototypical and smart material that undergoes a thermally driven amorphous-to-crystalline phase transition at the temperature above 433 K, which takes the material GST from an amorphous state to a polycrystalline cubic state [13]. The thermal control of the phase transition is generally achieved by either photothermal heating or electrical Joule heating [13]. To visualize, we utilize a photothermal heating method to demonstrate the temporal variation of temperature of the GST region for the MMPA and the planar control device by a heat transfer model using the finite element method (FEM) solver within the COMSOL software package.

As previously described, the large imaginary part of refractive index of GST leads to quite strong light absorption in MMPA, which will allow rapidly heating of the GST region to yield a fast phase transition from the amorphous to crystalline state. The involved material thermal properties used for the simulation are summarized in Table 1. The thermal conductivity of GST dependence on temperature is achieved by experimental data in [43]. In the heat transfer model, supercontinuum lasers were used as the excitation source. The wavelength range of the laser is from 500 to 2400 nm in which the power of the laser is evenly distributed [39]. The laser can emit the nanosecond (ns) pulse, which is a typical Gaussian profile. The incident Gaussian light beam has a repetition rate of $f_r = 25$ kHz and pulse duration of 0.15 ns. The light fluence irradiating on the unit cell from a single pulse can be written as [13,39]

Table 1. Material Thermal Properties Used in the Heat Transfer Model

	Special Heat Capacity Cs (J/(kg*K))	Density ρ(kg/m^3)	Thermal Conductivity k(W/(m*K))
Gold	129 [42]	19,300 [42]	317 (bulk) [42] 110(thickness = 100 nm) [42]
GST	220 [43]	6150 [43]	Temperature dependence [43]
Silica	741 [39]	2200 [39]	1 [39]
Air	1 [39]	353[K]/T [39]	0.03 [39]

$$F_l(r) = \frac{2P_0}{\pi w_0^2 f r}\exp\left(\frac{-2r^2}{w_0^2}\right), \quad (3)$$

where $P_0 = 0.35$ mW, representing the total power of a single pulse of the incident light shining on the sample, r is the distance from the Gaussian beam center, and $w_0 = 10$ μm is the Gaussian beam waist. Because the area of Gaussian beam waist far exceeds the unit cell area of the proposed MMPA structure, the light irradiating into the unit cell can be considered uniform with a light intensity of $I_0 = 1.11 \times 10^8$ W/m^2 (i.e., the amplitude of incident electric field $E_0 = 2.9 \times 10^5$ V/m). Therefore, the thermal energy absorbed by one unit cell is defined as [13,39]

$$E_{\text{th}}(r) = R_a p^2 F_l(r), \quad (4)$$

where R_a represents the absorption coefficient, 92.92% for MMPA and 56.96% for the planar control device, derived from the overlap between the light source power density spectrum and the metamaterial absorbance spectrum over the wavelength range from 350 to 1500 nm, as shown in Fig. 2(b). The heat source power is then expressed by a Gaussian pulse function as

$$Q_s(r,t) = \frac{E_{\text{th}}(r)}{\Delta V\sqrt{\pi}\tau}\exp\left(-\frac{(t-t_0)^2}{\tau^2}\right), \quad (5)$$

where ΔV is the volume of heat generation, $\tau = 0.15$ ns represents the temporal duration of the light pulse, $t_0 = 0.3$ ns is the time delay of the pulse peak. Figure 5(a) displays the heat source power $Q_s(r,t)$ for the two structures, where the structures are located at the center of the incident Gaussian light beam. It is found that the heat source power generated by the MMPA is far more than that by the planar control device. Meanwhile, Fig. 5(b) displays the comparison of temperatures in GST regions for the two structures. We can observe that the temperature of the GST cavity and the resonators in MMPA can reach 433 K (the phase transition temperature of GST) in just 0.37 ns and rise up to a maximum of 481 and 466 K after only 0.56 ns under the quite low incident intensity of 1.11×10^8 W/m^2. Due to heat dissipation and radiation to the surroundings, the temperature decreases after 0.56 ns before the next pulse injects. As a comparison, the maximum temperature of the GST region in the planar control device is only 418 K, which is lower than the phase transition temperature under the same incident power. A large temperature difference of 63 and 48 K at 0.56 ns within the corresponding GST regions between the MMPA and the planar control device indicates the high efficiency of MMPA for boosting the rate at which heat is delivered to GST regions. Note that the change in the optical properties during the phase transition of GST is not considered.

To gain deeper insight, the temperature distributions of the two structures at 0.56 ns are depicted in Figs. 5(c) and 5(d), respectively. One can see that the temperature within the GST cavity and GST resonators is approximately uniform due to their small sizes. Meanwhile, the temperature within

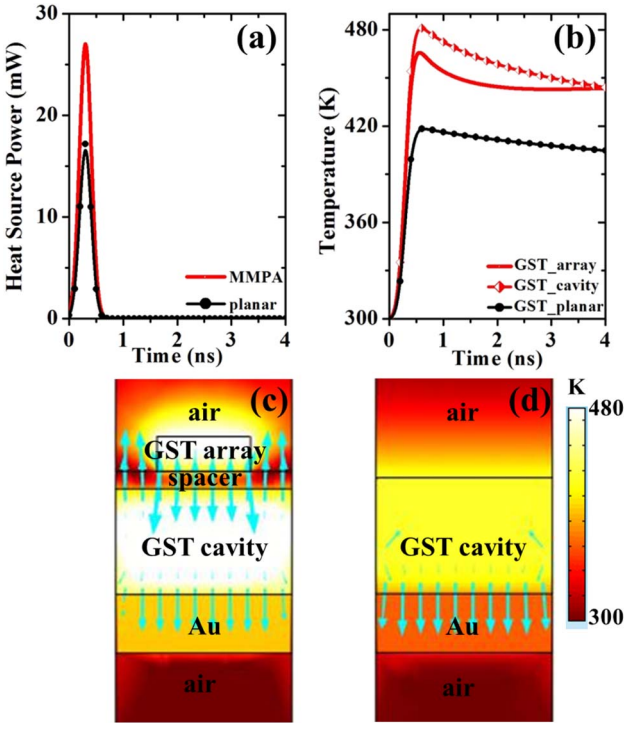

Fig. 5. (a) 3D-FEM simulation of heat power shining on the MMPA and the planar control device with amorphous GST located at the beam center, respectively. (b) Temperatures of GST square array in the MMPA and the GST cavity in the MMPA and the GST layer in the planar control device during one pulse. The cross section view of one unit cell of (c) MMPA and the (d) planar control device, where the color image indicates the temperature distribution, and the arrows indicate the heat flux at 0.56 ns.

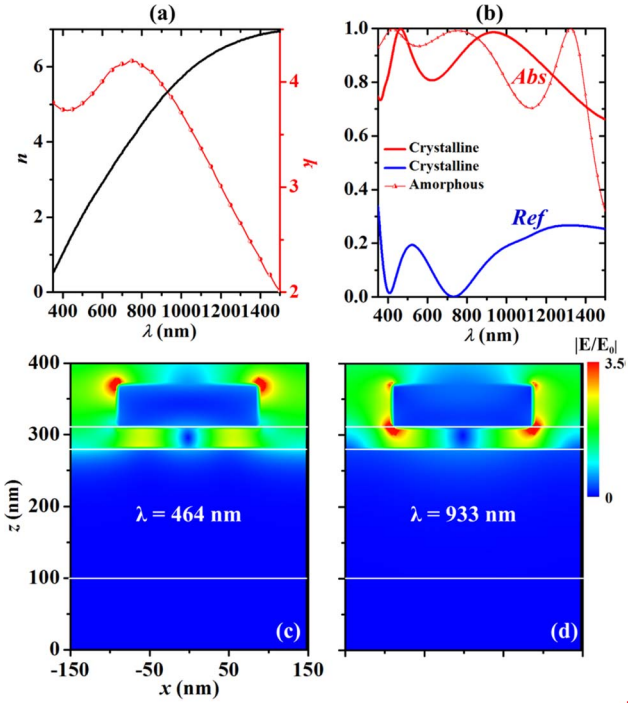

Fig. 6. (a) Real (solid line, black) and imaginary (symbol line, red) parts of the refractive index for crystalline GST. (b) 3D FDTD simulation of spectra of reflectance and absorbance for the proposed MMPA with crystalline GST at normal incidence. The absorption response of the proposed MMPA with amorphous GST also is given for comparison. (c)–(d) Normalized electric field distributions at the absorption peaks for the proposed MMPA with crystalline GST at normal incidence, respectively.

amorphous GST cavity of the MMPA is the highest. The cyan arrows representing total heat flux in both of the structures suggest that the dominant temperature gradient is along the same direction as the incident light, indicating that BK7 silica substrate is an effective heat sink [4].

As is described above, once the incident light with threshold intensity irradiates on the MMPA, the absorption/reflection properties of the scheme will be inevitably altered due to the phase transition of GST, which is a crucial reason for investigating the optical properties for the MMPA device after GST phase transition. Figure 6(a) shows the lineshape of the optical constant of GST after a phase transition. It can be observed that the crystalline GST also possesses a large imaginary part of the refractive index, indicating high absorption behaviors. To confirm this, we overlap the calculated reflectance and absorbance of the MMPA based on crystalline GST with the absorption response of the MMPA before phase transition (with amorphous GST) in Fig. 6(b). We find that, when switching the GST thin film to crystalline phase, the resonance feature is significantly redshifted, possibly due to more metal-like optical properties associated with the crystalline GST thin film [38]. Moreover, two resonant absorption peaks are found at the wavelength of 464 and 933 nm over the observed wavelength band. In order to investigate this optical absorption in this crystalline GST system, we calculate the electromagnetic field distributions at the absorption peaks, as shown in Figs. 6(c) and 6(d). Most of the electromagnetic field energy is confined at the corners of the GST array and the intermediate spacer due to the excitations of dipole and quadrupole resonances, which are analogous to the case of the MMPA before phase transition. In particular, comparing the refractive indices of GST in amorphous and crystalline states as well as referring to Eq. (2), we can speculate that, for the MMPA with crystalline GST, the third absorption peak due to GST cavity mode can still be produced under the incident light but redshifts far away from the wavelength region of interest. Furthermore, the integrated absorbance for the MMPA with crystalline GST over the whole wavelength can reach up to 86.2%, which verifies the feasibility of the proposed MMPA in the applications of solar cells and thermal photovoltaics.

5. CONCLUSION

In summary, we have demonstrated an MMPA design that exhibits near-perfect polarization-independent and broadband absorbance in the visible and NIR. By investigating the electromagnetic field distributions at the peaks of its absorption spectrum, we find the feature is attributed to the excitations of dipole/quadrupole resonances and cavity resonance due to the involvement of both resonators and cavity based on the GST PCM that possesses large real and imaginary parts of its dielectric constant. Furthermore, a heat transfer model is utilized to predict the temperatures of MMPA and the planar control device. We observe that, under a quite low incident light intensity of 1.11×10^8 W/m^2, the temperature of GST within MMPA can reach up to 433 K in just 0.37 ns and to 481 K at only 0.56 ns, which triggers the amorphous to crystalline phase transition of GST in a timescale of less than 1 ns. In comparison, the temperature of a reference planar control

device only rises up to 418 K, which is lower than the phase transition of GST. Therefore, such an MMPA offers a simple platform to achieve fast and energy-efficient optical devices based on phase transition materials and can be widely applied in biology, optical storage, and thermo-photovoltaic technology.

Funding. 973 Program of China (2013CB632704); National Natural Science Foundation of China (NSFC) (11374357, 11434017).

REFERENCES

1. N. Landy, S. Sajuyigbe, J. Mock, D. Smith, and W. Padilla, "Perfect metamaterial absorber," Phys. Rev. Lett. **100**, 207402 (2008).
2. W. Li and J. Valentine, "Metamaterial perfect absorber based hot electron photodetection," Nano Lett. **14**, 3510–3514 (2014).
3. H. A. Atwater and A. Polman, "Plasmonics for improved photovoltaic devices," Nat. Mater. **9**, 205–213 (2010).
4. Y. Cui, Y. He, Y. Jin, F. Ding, L. Yang, Y. Ye, S. Zhong, Y. Lin, and S. He, "Plasmonic and metamaterial structures as electromagnetic absorbers," Laser Photon. Rev. **8**, 495–520 (2014).
5. X. Lu, R. Wan, and T. Zhang, "Metal-dielectric-metal based narrow band absorber for sensing applications," Opt. Express **23**, 29842–29847 (2015).
6. Y. Li, B. An, S. Jiang, J. Gao, Y. Chen, and S. Pan, "Plasmonic induced triple-band absorber for sensor application," Opt. Express **23**, 17607–17612 (2015).
7. K. Bhattarai, Z. Ku, S. Silva, J. Jeon, J. O. Kim, S. J. Lee, A. Urbas, and J. Zhou, "A large-area, mushroom-capped plasmonic perfect absorber: refractive index sensing and Fabry-Perot cavity mechanism," Adv. Opt. Mater. **3**, 1779–1786 (2015).
8. D. R. Smith, J. B. Pendry, and M. C. Wiltshire, "Metamaterials and negative refractive index," Science **305**, 788–792 (2004).
9. V. M. Shalaev, "Optical negative-index metamaterials," Nat. photonics **1**, 41–48 (2007).
10. N. Liu, H. Guo, L. Fu, S. Kaiser, H. Schweizer, and H. Giessen, "Three-dimensional photonic metamaterials at optical frequencies," Nat. Mater. **7**, 31–37 (2008).
11. N. Liu, H. Liu, S. Zhu, and H. Giessen, "Stereometamaterials," Nat. Photonics **3**, 157–162 (2009).
12. E. Plum, V. Fedotov, P. Kuo, D. Tsai, and N. Zheludev, "Towards the lasing spaser: controlling metamaterial optical response with semiconductor quantum dots," Opt. Express **17**, 8548–8551 (2009).
13. T. Cao, C.-W. Wei, R. E. Simpson, L. Zhang, and M. J. Cryan, "Broadband polarization-independent perfect absorber using a phase-change metamaterial at visible frequencies," Sci. Rep. **4**, 3955 (2014).
14. X.-J. He, Y. Wang, J. Wang, T. Gui, and Q. Wu, "Dual-band terahertz metamaterial absorber with polarization insensitivity and wide incident angle," Prog. Electromagn. Res. **115**, 381–397 (2011).
15. H. Tao, C. Bingham, D. Pilon, K. Fan, A. Strikwerda, D. Shrekenhamer, W. Padilla, X. Zhang, and R. Averitt, "A dual band terahertz metamaterial absorber," J. Phys. D **43**, 225102 (2010).
16. Y. Ma, Q. Chen, J. Grant, S. C. Saha, A. Khalid, and D. R. Cumming, "A terahertz polarization insensitive dual band metamaterial absorber," Opt. Lett. **36**, 945–947 (2011).
17. J. W. Park, P. Van Tuong, J. Y. Rhee, K. W. Kim, W. H. Jang, E. H. Choi, L. Y. Chen, and Y. Lee, "Multi-band metamaterial absorber based on the arrangement of donut-type resonators," Opt. Express **21**, 9691–9702 (2013).
18. S. Li, J. Gao, X. Cao, Z. Zhang, Y. Zheng, and C. Zhang, "Multiband and broadband polarization-insensitive perfect absorber devices based on a tunable and thin double split-ring metamaterial," Opt. Express **23**, 3523–3533 (2015).
19. Y. Cheng, Y. Nie, and R. Gong, "A polarization-insensitive and omnidirectional broadband terahertz metamaterial absorber based on coplanar multi-squares films," Opt. Laser Technol. **48**, 415–421 (2013).
20. Y. Q. Ye, Y. Jin, and S. He, "Omnidirectional, polarization-insensitive and broadband thin absorber in the terahertz regime," J. Opt. Soc. Am B **27**, 498–504 (2010).
21. Y. Cui, K. H. Fung, J. Xu, H. Ma, Y. Jin, S. He, and N. X. Fang, "Ultrabroadband light absorption by a sawtooth anisotropic metamaterial slab," Nano Lett. **12**, 1443–1447 (2012).
22. J. Grant, Y. Ma, S. Saha, A. Khalid, and D. R. Cumming, "Polarization insensitive, broadband terahertz metamaterial absorber," Opt. Lett. **36**, 3476–3478 (2011).
23. X. Liu, T. Tyler, T. Starr, A. F. Starr, N. M. Jokerst, and W. J. Padilla, "Taming the blackbody with infrared metamaterials as selective thermal emitters," Phys. Rev. Lett. **107**, 045901 (2011).
24. H. Hu, D. Ji, X. Zeng, K. Liu, and Q. Gan, "Rainbow trapping in hyperbolic metamaterial waveguide," in *CLEO: QELS_Fundamental Science* (2013), paper QTu2A. 4.
25. H.-M. Lee and J.-C. Wu, "Temperature controlled perfect absorber based on metal-superconductor-metal square array," IEEE Trans. Magn. **48**, 4243–4246 (2012).
26. D. Loke, T. Lee, W. Wang, L. Shi, R. Zhao, Y. Yeo, T. Chong, and S. Elliott, "Breaking the speed limits of phase-change memory," Science **336**, 1566–1569 (2012).
27. A. Redaelli, A. Pirovano, A. Benvenuti, and A. Lacaita, "Threshold switching and phase transition numerical models for phase change memory simulations," J. Appl. Phys. **103**, 111101 (2008).
28. V. Weidenhof, I. Friedrich, S. Ziegler, and M. Wuttig, "Laser induced crystallization of amorphous $Ge_2Sb_2Te_5$ films," J. Appl. Phys. **89**, 3168–3176 (2001).
29. T. Cao, C. Wei, R. E. Simpson, L. Zhang, and M. J. Cryan, "Rapid phase transition of a phase-change metamaterial perfect absorber," Opt. Mater. Express **3**, 1101–1110 (2013).
30. K. Makino, J. Tominaga, and M. Hase, "Ultrafast optical manipulation of atomic arrangements in chalcogenide alloy memory materials," Opt. Express **19**, 1260–1270 (2011).
31. G. Dayal and S. A. Ramakrishna, "Design of multi-band metamaterial perfect absorbers with stacked metal-dielectric disks," J. Opt. **15**, 055106 (2013).
32. J. Van de Groep and A. Polman, "Designing dielectric resonators on substrates: combining magnetic and electric resonances," Opt. Express **21**, 26285–26302 (2013).
33. L. Zou, W. Withayachumnankul, C. M. Shah, A. Mitchell, M. Klemm, M. Bhaskaran, S. Sriram, and C. Fumeaux, "Efficiency and scalability of dielectric resonator antennas at optical frequencies," IEEE Photon. J. **6**, 1–7 (2014).
34. T. Cao, L. Zhang, R. E. Simpson, and M. J. Cryan, "Mid-infrared tunable polarization-independent perfect absorber using a phase-change metamaterial," J. Opt. Soc. Am. B **30**, 1580–1585 (2013).
35. E. D. Palik, *Handbook of Optical Constants of Solids* (Academic, 1998).
36. B.-S. Lee and S. G. Bishop, "Optical and electrical properties of phase change materials," in *Phase Change Materials* (Springer, 2009), pp. 175–198.
37. S. Jahani and Z. Jacob, "All-dielectric metamaterials," Nat. Nanotechnol. **11**, 23–36 (2016).
38. Y. Chen, T. Kao, B. Ng, X. Li, X. Luo, B. Luk'yanchuk, S. Maier, and M. Hong, "Hybrid phase-change plasmonic crystals for active tuning of lattice resonances," Opt. Express **21**, 13691–13698 (2013).
39. X. Chen, Y. Chen, M. Yan, and M. Qiu, "Nanosecond photothermal effects in plasmonic nanostructures," ACS Nano **6**, 2550–2557 (2012).
40. B. Lee and Z. Zhang, "Design and fabrication of planar multilayer structures with coherent thermal emission characteristics," J. Appl. Phys. **100**, 063529 (2006).
41. W. Zhou, K. Li, C. Song, P. Hao, M. Chi, M. Yu, and Y. Wu, "Polarization-independent and omnidirectional nearly perfect absorber with ultra-thin 2D subwavelength metal grating in the visible region," Opt. Express **23**, A413–A418 (2015).
42. G. Chen and P. Hui, "Thermal conductivities of evaporated gold films on silicon and glass," Appl. Phys. Lett. **74**, 2942–2944 (1999).
43. M. Kuwahara, O. Suzuki, Y. Yamakawa, N. Taketoshi, T. Yagi, P. Fons, T. Fukaya, J. Tominaga, and T. Baba, "Measurement of the thermal conductivity of nanometer scale thin films by thermoreflectance phenomenon," Microelectron. Eng. **84**, 1792–1796 (2007).